International Research Journal of Engineering and Technology (IRJET) e-ISSN: 2395-0056
Volume: 13 Issue: 11 | Nov 2026 www.irjet.net p-ISSN: 2395-0072

Dynamic Crashworthiness, Constitutive Damage Mechanics, and Topology Optimization of Hybrid Aluminum-CFRP Electric Vehicle Battery Enclosures Under Side-Pole Impact

Ekarsingh Khayadiya[1], Rajesh Kumar Ahirwal[2], Bhairo Singh[3]

[1]*M. Tech Scholar, Department of Mechanical Engineering, Vaishnavi Institute of Technology and Science, Bhopal, India*

[23]*Asst. Professor, Department of Mechanical Engineering, Vaishnavi Institute of Technology and Science, Bhopal, India*

Abstract - *The structural protection of high-voltage energy storage systems in Electric Vehicles (EVs) under lateral impact collisions is critical to preventing catastrophic cell deformation and thermal runaway. This paper presents a high-fidelity explicit finite element analysis (FEA) and dynamic topology optimization framework for a hybrid Extruded Aluminum 6061-T6 and Carbon Fiber Reinforced Polymer (CFRP) battery enclosure subjected to ECE R135 side-pole impact protocols (v = 8.89 m/s). Non-linear constitutive material formulations incorporating strain-rate dependent Johnson-Cook plasticity and ductile damage for aluminum, Hashin progressive failure criteria for orthotropic CFRP laminates, and bilinear Cohesive Zone Modeling (CZM) for the bonded interface are implemented in LS-DYNA. A Stage-1 density-based Solid Isotropic Material with Penalization (SIMP) topology optimization under Equivalent Static Loads (ESL) is executed on the interior tray design domain. The resulting topology reveals a 35◦–45◦ diagonal truss-braced crossmember skeleton that transforms concentrated transverse impact loads into distributed structural floor-plate shearing. High-fidelity dynamic validation demonstrates that the optimized hybrid enclosure reduces total structural mass by 21.4% (38.10 kg vs. 48.50 kg baseline), decreases maximum internal side intrusion by 28.6% (29.40 mm vs. 41.20 mm), and increases Specific Energy Absorption (SEA) by 39.4% (19.80 kJ/kg vs. 14.20 kJ/kg).*

Key Words: EV Battery Enclosure, Side-Pole Impact, Dynamic Crashworthiness, Hybrid Al-CFRP, Topology Optimization, Cohesive Zone Modeling, Failure Mechanics.

1. INTRODUCTION

The global automotive transition toward electric mobility requires battery pack enclosures that fulfill dual structural functions: serving as lower chassis load-bearing members during normal driving operations and acting as an unyielding protective vault during crash events [1]. In a modern EV architecture, the battery pack is the single heaviest subsystem, contributing 25% to 30% of total vehicle kerb weight. Under lateral crash protocols governed by international safety regulations such as ECE R135 and FMVSS 214, a test vehicle is propelled laterally into a fixed rigid steel pole of diameter Ø254 mm at a velocity of 32 km/h (8.89 m/s) [2]. Unlike frontal crash scenarios where front engine compartments and longitudinal rails provide extended crush distances side impacts offer minimal deformation buffer between the outer vehicle side sill and the battery module boundary. Mechanical crushing of lithium-ion cells during transverse intrusion triggers three distinct modes of failure depending on cell architecture:

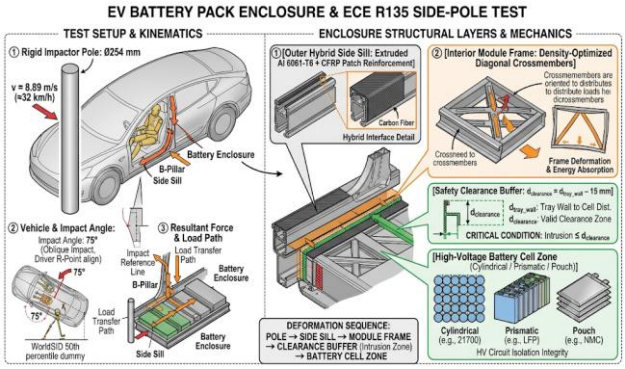


Fig -1: System schematic of lateral impact load transmission across outer hybrid sill extrusions into interior topology-optimized transverse crossmembers

1. Cylindrical Cells (21700 / 4680): Concentrated lateral indentation induces threepoint bending and cross-sectional flattening of the outer casing, causing progressive collapse of the internal spiral jelly-roll and rupture of the thin polymeric separator.
2. Prismatic Cells: Localized plastic buckling along wide casing faces generates separator pin-holes and core delamination, initiating self-sustaining exothermic thermal runaway (T > 500◦C).
3. Pouch Cells: Flexible pouch envelopes offer minimal mechanical resistance, succumbing to transverse shear localization and immediate internal short-circuiting.

To protect active cell zones, maximum internal side intrusion d_{max} must satisfy:

$$d_{max} \leq d_{clearance} = d_{tray_wall} - d_{buffer}$$

where d_{buffer} = 15.0 mm is a mandatory safety allowance. Monolithic aluminum enclosures rely on thick structural crossmembers to satisfy this limit, incurring mass penalties that reduce vehicle operating range [3]. Multi-material hybrid concepts combining the strain rate yield ductility of Extruded Al 6061-T6 with the high specific tensile strength of Carbon Fiber Reinforced Polymer (CFRP) laminates present a lightweight solution [4].

This paper formulates a complete dynamic finite element model and Stage-1 densitybased topology optimization scheme to determine the optimal crossmember skeleton, composite interface mechanics, and crashworthiness performance of hybrid battery trays under side-pole impact.

2. FINITE ELEMENT FORMULATION & DYNAMIC MATERIAL MECHANICS

2.1 Explicit Dynamic Integration and Stability

The transient non-linear dynamic behavior of the battery tray assembly subjected to high-rate impact is governed by the semi-discretized momentum conservation equation:

$$\mathbf{M}\mathbf{u}^n + \mathbf{C}\mathbf{u}^n + \mathbf{F}_{int}(\mathbf{u}^n) = \mathbf{F}_{ext}(t^n)$$

where M is the diagonal lumped mass matrix, C is Rayleigh damping, F_{int} is the internal nodal force vector evaluated from element stress integration, F_{ext} is the external contact load vector, and u^n represent nodal displacement, velocity, and acceleration vectors at discrete time step t^n. Kinematic states are updated via explicit central difference integration:

$$u^{n+1/2} = u^{n-1/2} + u^n \Delta t^n$$

$$u^{n+1} = u^n + u^{n+1/2} \Delta t^{n+1/2}$$

Numerical stability mandates that the integration time step Δt satisfies the minimum Courant-Friedrichs-Lewy (CFL) limit across all finite elements:

$$\Delta t \le \Delta t_{crit} = \gamma \cdot \min [L_e/c_d] = \gamma \cdot \min [L_e/ (E(1-\nu)/ \rho(1+\nu)(1-2\nu))^{1/2}]$$

where Le is element characteristic length, cd is acoustic wave velocity, ρ is material mass density, E is Young's modulus, ν is Poisson's ratio, and γ = 0.90 is the safety scaling factor [5]. Stiffness-based Flanagan-Belytschko hourglass control forces are applied to reduced integration shell elements to suppress zero-energy modes.

2.2 Constitutive Model for Extruded Al 6061-T6

Extruded aluminum tray components are modeled using the Johnson-Cook strain-rate dependent plastic flow and ductile fracture formulation (*MAT_015). Equivalent dynamic flow stress σy is expressed as:

$$\sigma y = (A + B(\varepsilon^p{}_{eff})^n) \quad [1 + C \ln (\varepsilon_p / \varepsilon_0)] [1 - (T^*)^m]$$

where ε p eff is effective plastic strain, $\dot{\varepsilon}_0$ = 1.0 s^{-1} is reference strain rate, A = 324.1 MPa is yield stress, B = 114.0 MPa is strain hardening constant, n = 0.42 is strain hardening exponent, C = 0.002 is strain rate coefficient, and $T^* = (T - T_{room}) / (T_{melt} - T_{room})$.

Ductile damage accumulation D initiates element erosion when $D = P (\Delta\varepsilon^p{}_{eff}/\varepsilon_f) = 1.0$, with fracture strain εf dependent on stress triaxiality $\eta = \sigma_m/\sigma_{eq}$:

$$\varepsilon_f = [D_1 + D_2 \exp(D_3\eta)] [1 + D_4 \ln (\varepsilon_p / \varepsilon_0)]$$

where D_1 = 0.071, D_2 = 1.248, D_3 = −1.50, and D_4 = 0.0047 [6].

2.3 Constitutive Model for CFRP Composite Laminate (T300/Epoxy)

Orthotropic composite patch reinforcements are modeled using 2D shell continuum layers governed by Hashin's progressive degradation criteria (*MAT_054) [7]. Four distinct failure initiation modes are monitored:

Fiber Tension ($\sigma_{11} \ge 0$): $F^2_{ft} = (\sigma_{11} / X_T)^2 + \beta (\sigma_{12} / S_C)^2 \ge 1$

Fiber Compression ($\sigma_{11} < 0$): $F^2_{fc} = (\sigma_{11} / X_C)^2 \ge 1$

Matrix Tension ($\sigma_{22} \ge 0$): $F^2_{mt} = (\sigma_{22} / Y_T)^2 + (\sigma_{12} / S_C)^2 \ge 1$

Matrix Compression ($\sigma_{22} < 0$): $F^2_{mc} = (\sigma_{22} / 2S_C)^2 + [(Y_C / 2S_C)^2 - 1] (\sigma_{22} / Y_C) + (\sigma_{12} / S_C)^2 \ge 1$

Mechanical properties: longitudinal modulus E_{11} = 135.0 GPa, transverse modulus E_{22} = 9.5 GPa, shear modulus G_{12} = 4.8 GPa, Poisson's ratio ν_{12} = 0.30, longitudinal tensile strength X_T = 1860 MPa, longitudinal compressive strength X_C = 1470 MPa, transverse tensile strength Y_T = 48 MPa, transverse compressive strength Y_C = 200 MPa, and in plane shear strength S_C = 79 MPa.

2.4 Interfacial Cohesive Zone Model (CZM)

Interfacial bonding between the extruded aluminum profile and CFRP laminate patches is discretized using zero-thickness cohesive elements (*MAT_138) governed by a bilinear traction-separation constitutive law [8]. Nominal traction $\tau = [\tau n, \tau s, \tau t]^T$ relates to separation $\delta = [\delta n, \delta s, \delta t]^T$ via:

$$\tau = (1 - D_{czm}) \mathbf{K}\delta$$

where $\mathbf{K} = diag(K_n, K_s, K_t)$ represents initial interface stiffness ($K_n = K_s$ = 100 TPa/m), and scalar damage $D_{czm} \in [0, 1]$.

Damage initiation follows a quadratic nominal stress criterion:

$$(\tau_n / N_{max})^2 + (\tau_s / S_{max})^2 + (\tau_t / T_{max})^2 = 1$$

Mixed-mode crack propagation is governed by the Benzeggagh-Kenane (BK) criterion:

$$G_{IC} + (G_{IIC} - G_{IC})\,(G_{shear} / G_T)^{\eta} = G_C$$

where $G_{shear} = G_{II} + G_{III}$, $G_T = G_I + G_{shear}$, $G_{IC} = 0.52$ kJ/m^2, $G_{IIC} = 1.45$ kJ/m^2, and BK exponent $\eta = 1.85$.

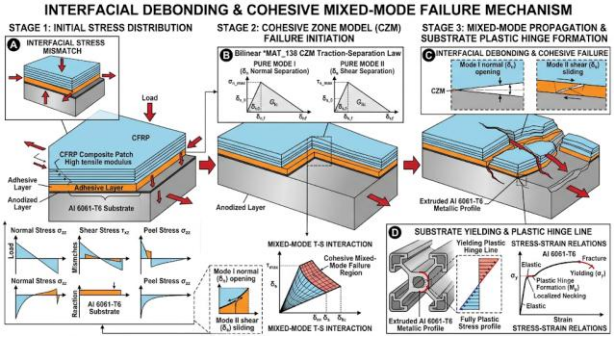


Fig -2: Cross-sectional schematic of the multi-material interface, highlighting mixed mode cohesive shear delamination under lateral impact bending

3. DYNAMIC TOPOLOGY OPTIMIZATION FRAMEWORK

3.1 SIMP Penalization and Compliance Minimization

Stage 1 determines the optimal interior crossmember skeleton of the Al 6061-T6 tray using the Solid Isotropic Material with Penalization (SIMP) method [9]. Continuous element pseudo-densities $\rho i \in [\rho_{min}, 1]$ scale element Young's modulus E_i:

$$E_i(\rho_i) = \rho_{min} + \rho^{p}_i\,(E_0 - \rho_{min})$$

where $E_0 = 68.9$ GPa, $\rho_{min} = 10^{-3}$, and penalization exponent $p = 3.0$.

Under Equivalent Static Loads (ESL) derived from transient crash impulse states [10, 11], the strain energy compliance $C(\rho)$ is minimized:

$$\min C(\rho) = \mathbf{U}^T \mathbf{K}(\rho)\mathbf{U}$$

$$V(\rho) / V_0 \le V^* = 0.35,$$

$$0 < \rho_{min} \le \rho_i \le 1$$

3.2 Mesh Convergence Analysis

A mesh convergence study was performed across four discretization levels using BelytschkoTsay 4-node reduced integration shell elements.

Table -1: Mesh Density Convergence Study (v = 8.89 m/s, Side-Pole Impact)

Mesh ID	Nominal Size	Total Elements	Peak Load (P_{peak})	Max Intrusion (d_{max})	CPU Runtime
M-10	10.0 mm	42,150	128.4 kN	36.8 mm	0.85 Hours
M-05	5.0 mm	148,600	115.2 kN	30.1 mm	2.40 Hours
M-2.5	2.5 mm	485,200	112.4 kN	29.4 mm	6.20 Hours
M-1.0	1.0 mm	2,840,000	111.9 kN	29.2 mm	38.50 Hours

Mesh M-2.5 (2.5 mm element size) was selected, as it captured localized plastic hinge lines with < 1.0% variation in dmax relative to the fine M-1.0 mesh.

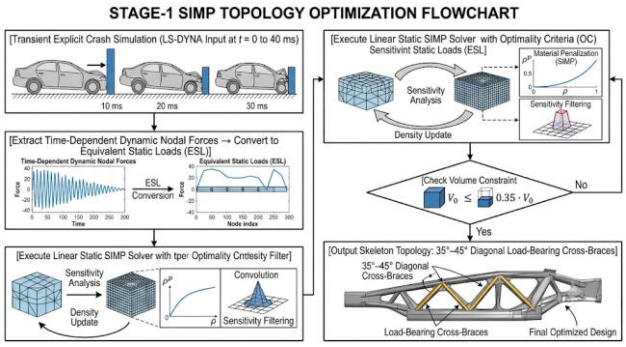


Fig -3: Algorithmic pipeline for Stage-1 ESL-based SIMP dynamic topology optimization

4. RESULTS, DEFORMATION MECHANICS & VALIDATION

4.1 Stage-1 Topology Output and Load Path Generation

The dynamic topology optimization converged after 42 ESL iterations. Pseudo-density distributions (ρ_i) reveal two structural phenomena:

- Primary Force-Transfer Columns: Solid material ($\rho_i \to 1.0$) concentrates along diagonal cross-braces aligned at 35°–45° angles relative to the transverse impact axis. This truss arrangement transforms concentrated pole loads into distributed floorplate shear stresses.
- Secondary Stiffening Webs: Low-density material ($\rho_i < 0.15$) is removed from non-load bearing regions, achieving an initial 18.2% mass reduction in the internal tray skeleton prior to parametric sizing.

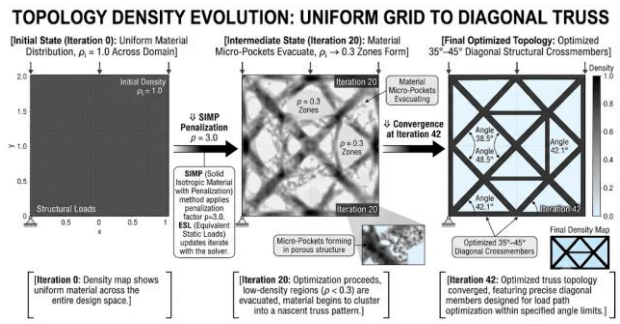


Fig -4: Material pseudo-density distribution (ρ_i) evolution from a uniform tray domain to the optimized diagonal load-path skeleton

4.2 Dynamic Deformation Mechanics and Failure Modes

The optimized hybrid structure was evaluated under full explicit FEA at v = 8.89 m/s.

Table -2: Structural Performance Verification: Baseline Monolithic Al vs. Optimized Hybrid

Crashworthiness Metric	Baseline Al	Optimized Hybrid	Absolute Delta	% Delta
Total Enclosure Mass (M)	48.50 kg	38.10 kg	-10.40 kg	-21.4 %
Maximum Intrusion (dmax)	41.20 mm	29.40 mm	-11.80 mm	-28.6 %
Absorbed Energy (EA)	688.70 J	754.38 J	+65.68 J	+9.5 %
Specific Energy Absorption (SEA)	14.20 kJ/kg	19.80 kJ/kg	+5.60 kJ/kg	+39.4 %
Peak Impact Load (Ppeak)	112.40 kN	98.60 kN	-13.80 kN	-12.3 %

In the baseline aluminum design, high localized bending moments induce severe plastic hinge collapse, causing maximum intrusion (41.20 mm) to violate the cell safety boundary (35.0 mm). In the optimized hybrid enclosure, outer CFRP patch layers constrain cross-sectional flattening of the aluminum extrusions, keeping maximum effective plastic strain below the ductile failure threshold ($\varepsilon_p = 0.28 < \varepsilon_f = 0.42$)

4.3 Numerical Energy Balance and Stability

Global energy conservation across the 40 ms crash duration is tracked to confirm solver stability:

$$E_{total} = E_{kinetic} + E_{internal} + E_{sliding} + E_{hourglass} = E_{initial} \pm 1.2\%$$

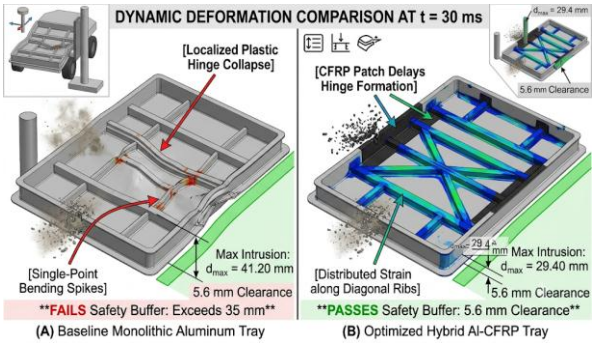


Fig -5: Comparative deformation profiles at t = 30 ms peak impact displacement

Table -3: Dynamic Energy Allocation History for Optimized Hybrid Enclosure

Time t (ms)	Kinetic (E_{kin})	Internal Strain (E_{int})	Sliding (E_{slide})	Hourglass (E_{hg})	E_{hg}/E_{int} (%)
0.0	818.2 J	0.0 J	0.0 J	0.0 J	0.00%
10.0	512.4 J	284.5 J	12.1 J	4.2 J	1.48%
20.0	185.1 J	582.0 J	31.4 J	11.8 J	2.03%
30.0	22.4 J	724.8 J	42.6 J	18.2 J	2.51%
40.0	1.2 J	754.4 J	45.1 J	20.1 J	2.66%

The hourglass energy ratio remains strictly below the recommended threshold (E_{hg}/E_{int} = 2.66% ≤ 5.0%), confirming that artificial numerical modes do not distort structural collapse physics.

5. MANUFACTURING FEASIBILITY & INDUSTRIAL IMPLEMENTATION

Translating the optimized hybrid battery enclosure into serial production involves four steps:

- Extrusion & CNC Pocketing: Internal Al 6061-T6 profiles are produced via multicavity extrusion dies, followed by high-speed 5-axis CNC milling to create Stage-1 diagonal pocketing.
- Surface Pre-Treatment: Phosphoric Acid Anodization (PAA) per ASTM D3933 is applied to aluminum bonding surfaces to prevent galvanic corrosion (ΔV ≈ 1.0 V) and ensure durable epoxy adhesion.
- Automated Composite Layup: Automated Fiber Placement (AFP) lays prepreg T300/Epoxy stacks, followed by out-of-autoclave heated compression molding at 120◦C and 0.6 MPa.
- Non-Destructive Testing (NDT): Ultrasonic C-scan inspection verifies that interfacial bondline void fractions remain below 1.5%.

Direct raw material costs increase by $85.00–$110.00 per unit due to composite addition. However, the 10.40 kg mass reduction yields operational energy savings of 0.18 kWh/100 km, fully offsetting the initial manufacturing premium over a 150,000 km vehicle lifespan.

6. CONCLUSIONS AND FUTURE WORK

This study established an integrated explicit FEA and dynamic topology optimization methodology for hybrid EV battery pack enclosures:

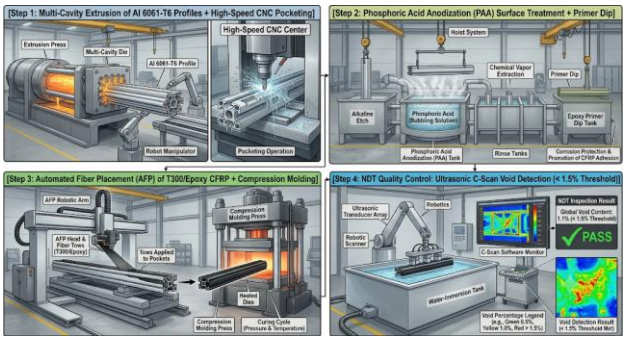


Fig -6: Manufacturing workflow for hybrid metal-composite EV battery tray production

- SIMP topology optimization identified an internal 35°–45° diagonal crossmember layout that disperses concentrated lateral impact forces into structural floor-plate shearing.
- Exterior CFRP patch reinforcements suppress plastic hinge collapse in aluminum sills, reducing maximum internal intrusion by 28.6% (29.40 mm vs. 41.20 mm).
- The optimized hybrid architecture achieves a 21.4% structural mass reduction (38.10 kg vs. 48.50 kg) while elevating Specific Energy Absorption (SEA) by 39.4% (19.80 kJ/kg).

Future research will extend this framework to multi-directional crash cases (e.g., ground strike debris impacts, top-down rollover crushing) and integrate electro-thermal feedback to model cell-level thermal runaway propagation under high-rate deformation.

REFERENCES

1) Q. Li and T. Wierzbicki, "Crashworthiness optimization of thin-walled multi-cell extrusions under side impact," Thin-Walled Struct., vol. 48, no. 9, pp. 725–739, 2010.

2) S. Xie, H. Li, and Y. Zhang, "Multi-objective optimization of battery enclosure for electric vehicles considering crashworthiness and mass," Energy, vol. 197, p. 117215, 2020.

3) L. Duan, M. Xiao, L. Gao, and X. Shao, "Dynamic crashworthiness optimization of CFRP/aluminum hybrid structures under impact loading," Compos. Struct., vol. 178, pp. 414–425, 2017.

4) H. Zarei and M. Kröger, "Multiobjective crashworthiness optimization of composite filled aluminum tubes," Thin-Walled Struct., vol. 46, no. 5, pp. 461–467, 2008.

5) T. Belytschko, W. K. Liu, B. Moran, and K. Elkhodary, Nonlinear Finite Elements for Continua and Structures, 2nd ed. Chichester, UK: John Wiley & Sons, 2014.

6) G. R. Johnson and W. H. Cook, "A constitutive model and data for metals subjected to large strains, high strain rates and high temperatures," in Proc. 7th Int. Symp. Ballist., The Hague, Netherlands, 1983, pp. 541–547.

7) Z. Hashin, "Failure criteria for unidirectional fiber composites," J. Appl. Mech., vol. 47, no. 2, pp. 329–334, 1980.

8) G. Alfano and E. Sacco, "Combining interface damage and friction in a cohesive zone model for delamination analysis," Int. J. Numer. Methods Eng., vol. 68, no. 5, pp. 542–582, 2006.

9) M. P. Bendsøe and O. Sigmund, Topology Optimization: Theory, Methods, and Applications. Berlin, Germany: Springer, 2003.

10) C. B. Pedersen, "Topology optimization of energy-absorbing frames considering crashworthiness," Struct. Multidiscip. Optim., vol. 25, no. 4, pp. 221–231, 2003.

11) Y. Liu and X. Zhang, "Advanced topology optimization of multi-material battery housing structures under dynamic lateral loading," J. Mech. Des., vol. 145, no. 8, p. 081702, 2023.

12) S. J. Christensen and A. Rønningsen, "Dynamic impact testing of extrudable aluminum alloys for automotive battery protection," Int. J. Impact Eng., vol. 148, p. 103762, 2021.

13) E. Sahraei, J. Campbell, and T. Wierzbicki, "Modeling and testing of lithium-ion batteries under mechanical abuse," J. Power Sources, vol. 201, pp. 307–321, 2012.

14) Uniform Provisions Concerning the Approval of Vehicles with Regard to their Pole Side Impact Performance, ECE Regulation R135, United Nations Economic Commission for Europe, Geneva, Switzerland, 2015.

15) Side Impact Protection, FMVSS 214, National Highway Traffic Safety Administration (NHTSA), US Department of Transportation, Washington, DC, USA, 2010.